Chemical vapor deposition of Fe-N-C oxygen reduction catalysts with full utilization of dense Fe-N_4 sites

Li Jiao[1], Jingkun Li[2], Lynne LaRochelle Richard[3], Qiang Sun[3], Thomas Stracensky[3], Ershuai Liu[3], Moulay Tahar Sougrati[2], Zipeng Zhao[4], Fan Yang[5], Sichen Zhong[5], Hui Xu[5], Sanjeev Mukerjee[3], Yu Huang[4,6], David A. Cullen[7], Deborah J. Myers*[,8], Frédéric Jaouen*[,2], and Qingying Jia*[,3]

[1]Department of Chemical Engineering, Northeastern University, Boston, Massachusetts, 02115, United States

[2]ICGM, Univ. Montpellier, CNRS, ENSCM, Montpellier, France

[3]Department of Chemistry and Chemical Biology, Northeastern University, Boston, Massachusetts, 02115, United States

[4]Department of Materials Science and Engineering, University of California, Los Angeles, California, 90095, United States

[5]Giner, Inc, Newton, Massachusetts, 02466, United States

[6]California NanoSystems Institute (CNSI), University of California, Los Angeles, California, 90095

[7]Center for Nanophase Materials Sciences, Oak Ridge National Laboratory, Oak Ridge, Tennessee 37831, USA

[8]Chemical Sciences and Engineering Division, Argonne National Laboratory, Lemont, Illinois, 60439, United States

*Correspondence authors. Emails: dmyers@anl.gov (D. M.); frederic.jaouen@umontpellier.fr (F. J.); q.jia@northeastern.edu (Q. J.)

One Sentence Summary: A Fe-N-C catalyst synthesized via chemical vapor deposition exhibits a record Fe-N_4 site density with 100% site utilization and record performance in fuel cells.

Abstract. Replacing scarce and expensive platinum (Pt) with metal-nitrogen-carbon (M-N-C) catalysts for the oxygen reduction reaction (ORR) in proton exchange membrane fuel cells (PEMFCs) has largely been impeded by the low activity of M-N-C, in turn limited by low site density and low site utilization. Herein, we overcome these limits by implementing chemical vapor deposition (CVD) to synthesize Fe-N-C, an approach fundamentally different from previous routes. The Fe-N-C catalyst, prepared by flowing iron chloride vapor above a N-C substrate at 750 °C, has a record Fe-N_4 site density of 2×10^{20} sites·gram^{-1} with 100% site utilization. A combination of characterizations shows that the Fe-N_4 sites formed via CVD are located exclusively on the outer-surface, accessible by air, and electrochemically active. This catalyst delivers an unprecedented current density of 33 mA·cm^{-2} at 0.90 $V_{iR\text{-free}}$ (*iR*-corrected) in an H_2-O_2 PEMFC at 1.0 bar and 80 °C.

The commercialization of hydrogen fuel cell vehicles (FCVs) initiated in Japan in 2014 has, since then, spread to only a few additional countries. In addition to the currently limited hydrogen fueling infrastructure, another major barrier to the global commercialization of FCVs is the high cost of the proton exchange membrane fuel cell (PEMFC) stack (*1*). This high cost originates largely from the high platinum loading in the cathode, needed to activate the sluggish oxygen reduction reaction (ORR) (*2*). From a catalysis perspective, the two major routes to reducing the platinum content of a PEMFC stack are improving the mass activity of Pt-based catalysts or replacing Pt with less expensive catalysts based on more abundant metals and, in particular, free of platinum group metals (PGM-free). The U.S. Department of Energy (DOE) has set a 2025 ORR activity target for PGM-free catalysts in a PEMFC of 44 $mA \cdot cm^{-2}$ at 0.90 V cell voltage, after Ohmic drop correction (*i*R-free), with 1.0 bar H_2 and O_2 on the anode and cathode, respectively (*3*). This, along with performance on H_2 and air feeds, is a key descriptor for the performance of PGM-free cathodes in PEMFCs.

The leading PGM-free ORR catalysts are pyrolyzed transition metal-nitrogen-carbon (M-N-C, M=Fe or Co) materials (*4-10*). Highly active Fe-N-C catalysts have been produced by various methods such as hard templating (silica) (*11, 12*) and soft templating (polymer and organic compounds (*4, 13*), Zn-based metal organic framework (MOF) (*7, 9, 14, 15*)). All these methods incorporate the core feature of the synthesis route initiated by Yeager *et al*. in 1989 (*16*), that is, pyrolyzing at 900-1100 °C a catalyst precursor that comprises Fe, N, and C elements. From structural characterizations, it has been identified that all the pyrolyzed Fe-N-C catalysts share similar Fe-N_4 sites (*14, 17-19*), formed during the

pyrolysis step (*17*). The ORR activity in acid medium of these Fe-N-C catalysts is limited by both the low turnover frequency (TOF) and low density of gas-phase accessible Fe-N_4 sites *per* mass of Fe-N-C (SD_{mass}) (*20*). Primbs *et al.* (*20*) recently determined four benchmark Fe-N-C catalysts the SD_{mass} via CO chemisorption and the ensuing average TOF. Among this set of benchmark catalysts, both the highest SD_{mass} (~6×10^{19} sites·g^{-1}) and highest TOF (~0.7 $e^{-}.site^{-1}.s^{-1}$ at 0.8 V) are approximately one order of magnitude lower than that of Pt/C (*21, 22*). Thus, improving the TOF and/or SD_{mass} of Fe-N-C catalysts are effective pathways to advancing their ORR activity. However, it is currently unclear how to rationally improve the TOF of Fe-N_4 sites prepared via pyrolysis. Developing other PGM-free sites with higher TOFs may be an alternative option. Recently, a Sn-N-C catalyst with Sn-N_x sites showed a similar TOF than Fe-N_4 sites in a parent Fe-N-C catalyst prepared similarly, but a lower SD_{mass} (*23*).

Increasing the SD_{mass} of M-N-C materials seems therefore to be currently the most feasible approach to increase their ORR activity. It faces however two challenges: i) the parallel formation during pyrolysis of Fe-N_4 sites and ORR-inactive or less active Fe species at high Fe content (*9, 15*), and ii) the uncontrolled location of Fe-N_4 sites, a fraction of them being buried in the bulk of the N-doped carbon matrix with current synthetic approaches, and therefore inaccessible by O_2. Related to the challenges i) and ii), we define two utilization sub-factors, $U_{Fe,}$ and U_{FeN4} the former being the ratio of the number of Fe atoms present as Fe-N_4 moieties to the total number of Fe atoms in a Fe-N-C catalyst, and the latter the ratio of gas-phase accessible Fe-N_4 moieties to all Fe-N_4 moieties in a catalyst. The SD_{mass} is related to $U_{Fe,}$, U_{FeN4}, and the Fe wt% by the equation:

$$SD_{mass} = \frac{Fe\ wt\%}{100 \times M_{Fe}} \times N_A \times U_{Fe} \times U_{FeN4} \quad (1)$$

Where Fe wt% is the total Fe content in Fe-N-C, M_{Fe} is the molar mass of iron; N_A is Avogadro's constant. The overall utilization factor, U, is defined as:

$$U = U_{Fe} \times U_{FeN4} \quad (2)$$

Developing a synthetic approach that favors the conversion of Fe into Fe-N_4 sites even at relatively high Fe content, while simultaneously favoring the location of Fe-N_4 sites on the outer-surface, is therefore acutely needed. As an example of the challenge i), Shui *et al*. (*12*) recently showed that the U of their Fe-N-C catalysts dramatically drops from 43.5% to ~11.4% as the Fe content increases from 0.3 wt% to 2.8 wt%, due to strong Fe clustering at high Fe content. This led to a maximum SD_{mass} of 3.4×10^{19} sites·g^{-1}, comparable to those of the benchmark Fe-N-C catalysts (*20*). As an example of the challenge ii), Primbs *et al.* (*20*) showed that the SD_{mass} values measured by CO-chemisorption of Fe-N-C catalysts with Fe being present only or mostly as Fe-N_4 sites are significantly lower than the total number of Fe-N_4 sites determined by ^{57}Fe Mössbauer spectroscopy. The SD_{mass} values reached only 20-45% of the bulk SD of Fe-N_4 sites (i.e. U_{FeN4} = 20-45%), except for the PAJ catalyst (U_{FeN4} ~ 80%). The latter, however, was characterized at the same time with a low U_{Fe} value, with Fe being present mainly as Fe particles (*20*). The low U_{Fe} and/or U_{FeN4} in Fe-N-C catalysts are related to the major approach for the synthesis of Fe-N-C catalysts applied hitherto that involves mixing or combining Fe, N, and C precursors first, and subjecting the catalyst precursor to high-temperature pyrolysis leading to the simultaneous transformation of N and C into a N-doped carbon matrix and of Fe, N and C into Fe-N_4 sites and/or Fe clusters. This

naturally results in that the formed Fe-N_4 sites are located rather uniformly throughout the N-doped microporous carbon (N-C) matrix. Those buried in the core are electrochemically inactive, leading to $U_{FeN4} << 100\%$. High Fe contents also reduce the U_{Fe} by graphitizing the N-C during pyrolysis, lowering the N-content, in turn decreasing the ability of N-C to accommodate Fe-N_4 sites (*9*). Therefore, the SD_{mass} of Fe-N-C catalysts is inherently limited when using the existing synthesis approaches. Increasing the SD_{mass} of Fe-N-C catalysts by developing new synthesis routes is, however, hindered by the poor understanding of the Fe-N_4 site formation mechanism during pyrolysis.

Our groups recently determined that Fe-N_4 sites are formed through gas phase diffusion of single iron atoms (Fe_1) in tetrahedral Fe-O_4 moieties into N_4-C cavities during pyrolysis (*17*). The ultrashort diffusion length of Fe_1 requires close proximity of Fe sources and N_4-C cavities, otherwise Fe_1 atoms nucleate forming Fe clusters during diffusion, as observed during the pyrolysis of Fe(II) acetate that is not in physical contact with the N-C substrate (*17*). This new understanding not only explains the necessity to sufficiently mix Fe precursor with N and C precursors to form Fe-N_4 sites with existing synthesis routes, but also points out the possibility of avoiding the mixing stage and minimizing the formation of Fe clusters by choosing Fe precursors with long diffusion lengths. Inspired by these new insights, herein we implement chemical vapor deposition (CVD) to flow iron chloride vapor above a bed of N-C powders to preferentially form Fe-N_4 sites on the outer-surface. The iron chloride vapor has a long diffusion length because the Fe atoms are individually surrounded by chloride ions, which prohibits iron atoms from nucleating during diffusion. Structural and electrochemical characterization confirm that a high density of Fe-N_4 sites are exclusively formed on the outer-surface of N-C,

accessible by air, leading to full utilization of Fe-N_4 sites (U_{FeN4} =100%). The catalyst synthesized at 750 °C exhibits an unprecedented ORR activity of 33 mA·cm^{-2} at 0.90 $V_{iR\text{-}free}$ and 44 mA·cm^{-2} at 0.89 $V_{iR\text{-}free}$ in an H_2-O_2 PEMFC, only 0.01 V lower than the DOE 2025 target (*3*).

Synthesis of Fe-N-C via CVD. To obtain a highly porous and nitrogen rich N-C substrate for the CVD, we first prepared a zeolitic imidazolate framework (ZIF-8) with a uniform crystal size of ~80 nm (Figure 1A) by dissolving $Zn(NO_3)_2 \cdot 6H_2O$ (0.1 M) and 2-methylimidazole (0.4 M) in methanolic solution, followed by centrifugation and vacuum drying of the collected powders. The X-ray diffraction (XRD) pattern of the synthesized ZIF-8 matches that of the pattern in the XRD database (JCPDS: 00-062-1030) (Figure 1B), verifying the exclusive formation of ZIF-8. The tetrahedral Zn-N_4 structure in ZIF-8 is confirmed by analysis of the Fourier-transform of the extended X-ray absorption fine structure (FT-EXAFS) spectrum at the Zn K-edge (Figure S1 and Table S1).

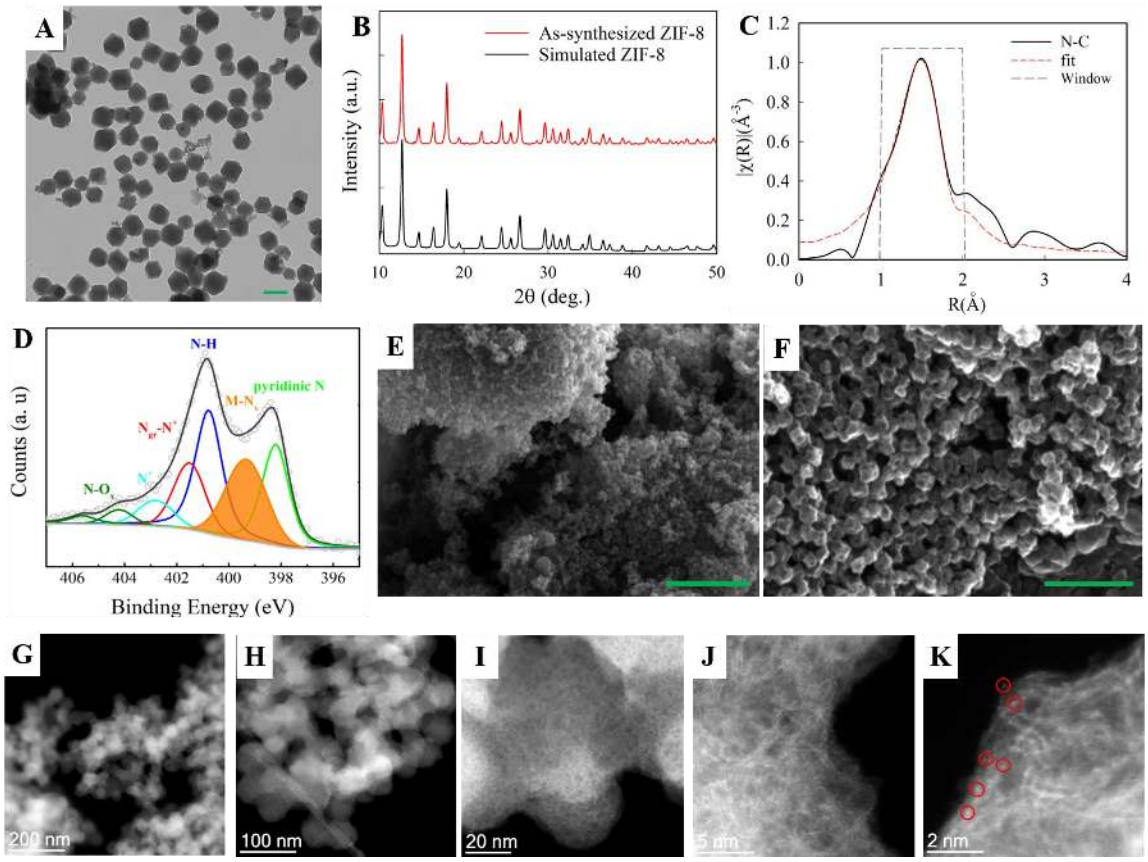

Figure 1. **Characterizations of the synthesized ZIF-8 and the ZIF-8 derived N-C substrate**. (**A**) Transmission electron microscopy (TEM) of ZIF-8. (**B**) XRD patterns of as-synthesized ZIF-8 and the simulated one (JCPDS: 00-062-1030). (**C**) Zn K-edge FT-EXAFS spectrum and fit of N-C. (**D**) High-resolution N_{1s} XPS of N-C. The assignments of different N species follow those in a recent work (*24*). (**E** and **F**) SEM images of the N-C. (**G-K**) ADF-STEM images of N-C with various scales. Residual Zn atoms are circled in red to guide the eye. The green scale bar in (A), (E), and (F) represents 100 nm, 1 μm, and 300 nm, respectively.

We then mixed the nanosized ZIF-8 (1.0 g) with 1,10 phenanthroline (0.25 g) in ethanol solution and dried the suspension. The generated dry powder was homogenized via low energy ball milling followed by pyrolysis under Ar at 1050 °C (*25*). The synthesized N-C contains 4.23 wt% of N and 2.16 wt% of Zn, as determined by inductively coupled plasma optical emission spectrometry (ICP-OES) (Table S2). Fitting of the Zn K-edge EXAFS data for the N-C shows that Zn is present in the form of $Zn\text{-}N_4$ with a Zn-N bond distance of 1.98±0.01 Å (Figure 1C and Table S1). The similar $Zn\text{-}N_4$ structure was recently reported by Jaouen *et al* (*26*) in a nitrogen-doped carbon prepared by flash

pyrolysis of ZIF-8 at 1050 °C, with or without mixing with a second transition metal. The existence of the Zn-N binding is also supported by fitting of the X-ray photoelectron spectroscopy (XPS) N_{1s} spectrum displayed in Figure 1D, wherein the peak at ~399.5 eV is commonly assigned to N bonded to a transition metal (*24*). The N-C has a Brunauer-Emmett-Teller (BET) area of 807 $m^2 \cdot g^{-1}$ and a microporous surface area of 692 $m^2 \cdot g^{-1}$. The high porosity of N-C is a result of the high initial microporosity of ZIF-8, plus the release of a large amount of Zn from ZIF-8 as Zn vapor during pyrolysis creates abundant voids inside the ZIF-8 crystals (*9, 14*). This is reflected by the scanning electron microscopy (SEM) images that manifest the preservation of the size and shape of the crystals of ZIF-8 upon pyrolysis and transformation into N-C particles (Figure 1E and 1F), despite the significant loss of the mass. Single Zn atoms embedded in the highly porous N-C can be directly visualized using aberration-corrected scanning transmission electron microscopy (AC-STEM) in annular dark-field (ADF) images (Figure 1G-K). Collectively, the N-C possesses abundant Zn-N_4 moieties embedded in a highly porous carbon matrix.

Anhydrous $FeCl_3$ (99%, Sigma-Aldrich) was chosen as the Fe source because its low boiling point, ~316 °C, allows for generation of iron chloride vapor at low temperature (*27, 28*). The $FeCl_3$ (80 mg) and N-C (80 mg) substrate were placed in two separate boats situated 1 cm apart in a quartz tube and pyrolyzed at 650 °C, 750 °C, 900 °C, or 1000 °C for three hours, followed by cooling to room temperature in the tube furnace (*25*). The furnace was continuously flowed with Ar gas with a flow rate of 0.65 $L \cdot min^{-1}$ during the heat treatment procedure.

Evaluation of the ORR activity and performance of FeNC-CVD-750. The ORR activities of the powders collected from the N-C boat (labelled as FeNC-CVD-T, where T represents the pyrolysis temperature in °C) were measured using a rotating disk electrode (RDE). Among the four catalysts, FeNC-CVD-750 exhibited the highest ORR activity (Figure S2) with a half wave potential of 0.85 V (all potentials here are versus reversible hydrogen electrode) when using a catalyst loading of 800 $\mu g \cdot cm^{-2}$ and oxygen-saturated 0.5 M H_2SO_4 (Figure 2A). The corresponding kinetic current density derived from the current at 0.8 V and the limiting current using the Koutecky-Levich equation is 20 $mA \cdot cm^{-2}$ or 25 $A \cdot g^{-1}$ (Figure 2B). These half-wave potential and mass activity values are among the highest reported for PGM-free catalysts in acidic electrolyte (*29*). The kinetic current density exhibits a Tafel slope of ~60 mV/dec above 0.8 V (Figure 2B), which has been commonly reported for Fe-N-C catalysts (*30, 31*). This Tafel slope is comparable to that of Pt-based catalysts (*22*), indicating that they share the same rate determining step for the ORR.

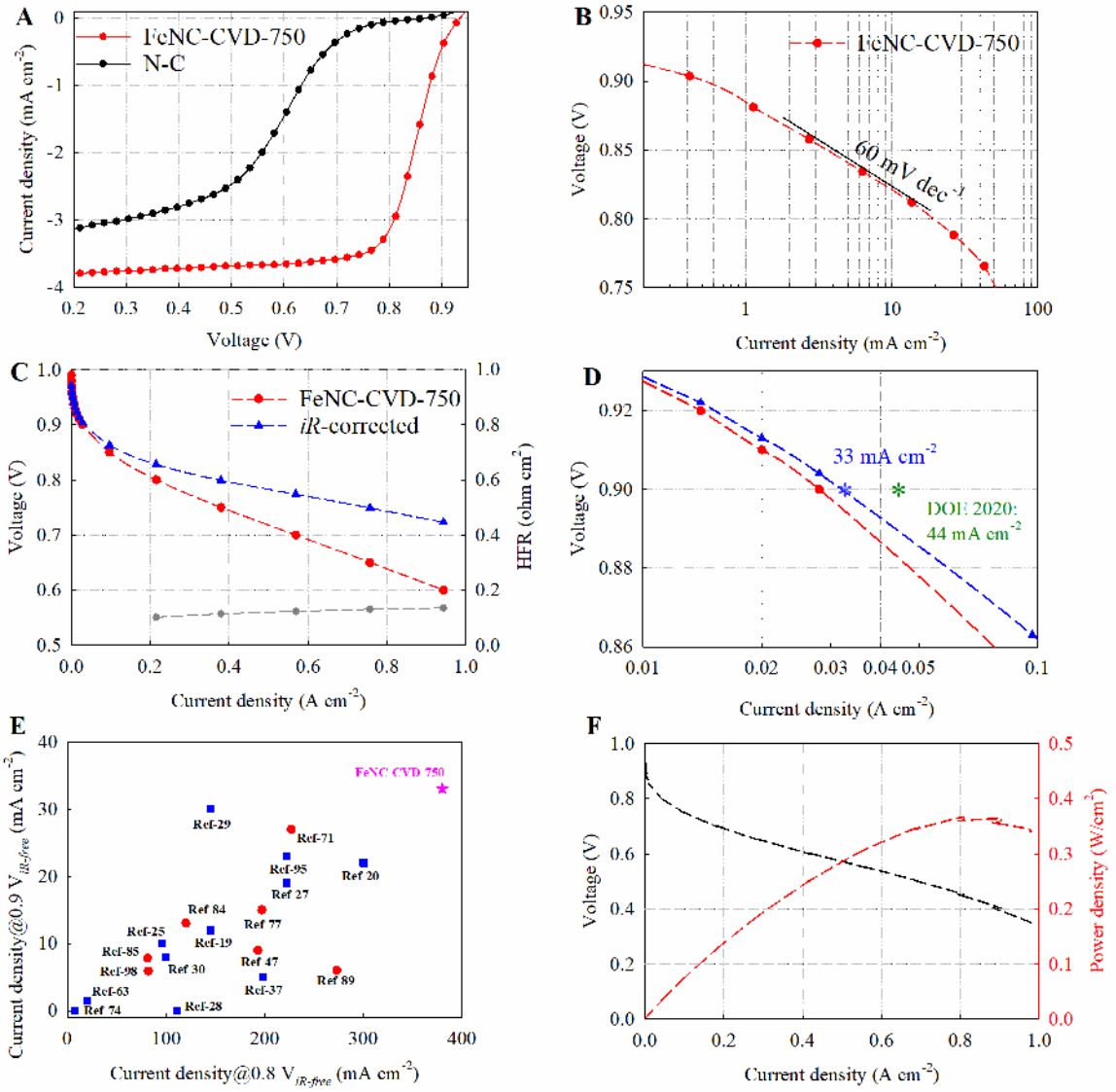

Figure 2. **ORR performance of FeNC-CVD-750 catalyst and electrode in PEMFCs**. (**A**) ORR polarization curve of the FeNC-CVD-750 catalyst. Steady-state RDE polarization curve in room-temperature, O_2-saturated 0.5 M H_2SO_4 using a rotation rate of 900 *rpm*, 20mV potential steps from 0.05 to 0.95 V, and a 25-s potential hold time at each step. (**B**) Tafel plots derived from the ORR polarization curves displayed in (A). (**C**) H_2-O_2 PEMFC polarization curves with and without *i*R-correction. Cathode: ~6.0 mg·cm^{-2} of the FeNC-CVD-750 catalyst; Anode: 0.3 mg$_{Pt}$·cm^{-2} Pt/C; Membrane: Nafion 212; 200 mL min^{-1} gas fed at the anode (H_2) and 1000 mL min^{-1} at the cathode (O_2) at 100% RH, 1.0 bar partial pressure H_2 and O_2, 80 °C, electrode area 5 cm^2. The grey dotted line represents the high frequency resistance (HFR). (**D**) Tafel plots derived from the ORR polarization curves displayed in (C) to illustrate the measured ORR activity at 0.9 V versus the DOE 2025 target. (**E**) Comparison of the H_2-O_2 PEMFC activity at 0.9 $V_{iR\text{-}free}$ and 0.8 $V_{iR\text{-}free}$ of FeNC-CVD-750 with literature values. The literature data and the corresponding reference numbers were directly collected from Ref [34]. The data points in blue were collected at 100% RH, 1.0 bar partial pressure of H_2 and O_2, 80 °C, whereas the data points in red were collected at 100% RH, 2.0 bar partial pressure of H_2 and O_2, 80 °C. (**F**) The H_2-air PEMFC

polarization curve and power density without *i*R-correction for the FeNC-CVD-750 MEA acquired after the H_2-O_2 polarization curves; 500 mL min^{-1} H_2 and 2000 mL min^{-1} air, 100% RH, 1.0 bar H_2 and air partial pressure, 80 °C.

The FeNC-CVD-750-containing electrode was evaluated in an H_2-O_2 PEMFC for three full polarization scans, followed by acquisition of H_2-air polarization curves on the same MEA. A current density of 44 mA·cm^{-2} is reached at 0.89 $V_{iR\text{-free}}$ during the first scan (increasing-current) in the H_2-O_2 PEMFC at 1.0 bar partial pressure of O_2 and 80 °C, 0.01 V lower than the DOE 2025 target (*3*) (Figure 2C and 2D). A current density of 33 mA·cm^{-2} was achieved at 0.9 $V_{iR\text{-free}}$ and 380 mA·cm^{-2} at 0.8 $V_{iR\text{-free}}$, both exceeding those of all previous PGM-free catalysts reported to date in H_2-O_2 PEMFCs under similar conditions (Figure 2E).

The current at 0.9 $V_{iR\text{-free}}$ drops to 22 mA·cm^{-2} and then 18 mA·cm^{-2} on the second and third scans, respectively (Figure S3) indicating that the FeNC-CVD-750 catalyst has poor stability in H_2-O_2 PEMFCs, similar to all highly active Fe-N-C catalysts (*32, 33*). This result is expected since all these Fe-N-C catalysts, including FeNC-CVD-750, likely share the same Fe-N_4 active sites (*17*). Despite the degradation, a maximum power density of 0.37 W·cm^{-2} was obtained in the subsequent H_2-air PEMFC testing (Figure 2F), which is among the highest values reported for PGM-free catalysts thus far (*34*).

Characterization of FeNC-CVD-750. To understand the source of its exceptional ORR activity, the FeNC-CVD-750 was characterized using multiple techniques. A representative SEM image of FeNC-CVD-750 (Figure 3A) shows a similar powder morphology to N-C (Figure 1F), without noticeable particle growth and aggregation. Meanwhile, the ADF- and secondary electron (SE)-STEM images, at different magnifications, show the highly porous morphology of the carbon matrix and absence of

metal clusters (Figure 3B-D). Moreover, the XRD pattern (Figure S4A), the C and N contents (Table S2), and the XPS N_{1s} spectrum (Figure 3E and Figure S4B) of FeNC-CVD-750 are nearly the same as those of the N-C. These results show that the overall morphology of the N-C is largely preserved after the CVD at 750 °C, which is expected considering that the N-C was synthesized using pyrolysis at 1050 °C prior to the CVD of Fe. On the other hand, the Zn content drops from 2.16 wt% in the N-C to 0.12 wt% in FeNC-CVD-750, accompanied by incorporation of 2.00 wt% Fe (Table S2). The presence of abundant Fe-N_x moieties in FeNC-CVD-750 is directly evidenced by atomic resolution ADF-STEM imaging coupled with electron energy loss spectroscopy (EELS). Abundant bright dots are clearly seen in the ADF-STEM image (Figure 2G, inset), for which the EELS point spectrum shows the close proximity of single Fe atom and N (Figure 2G and Figure S5).

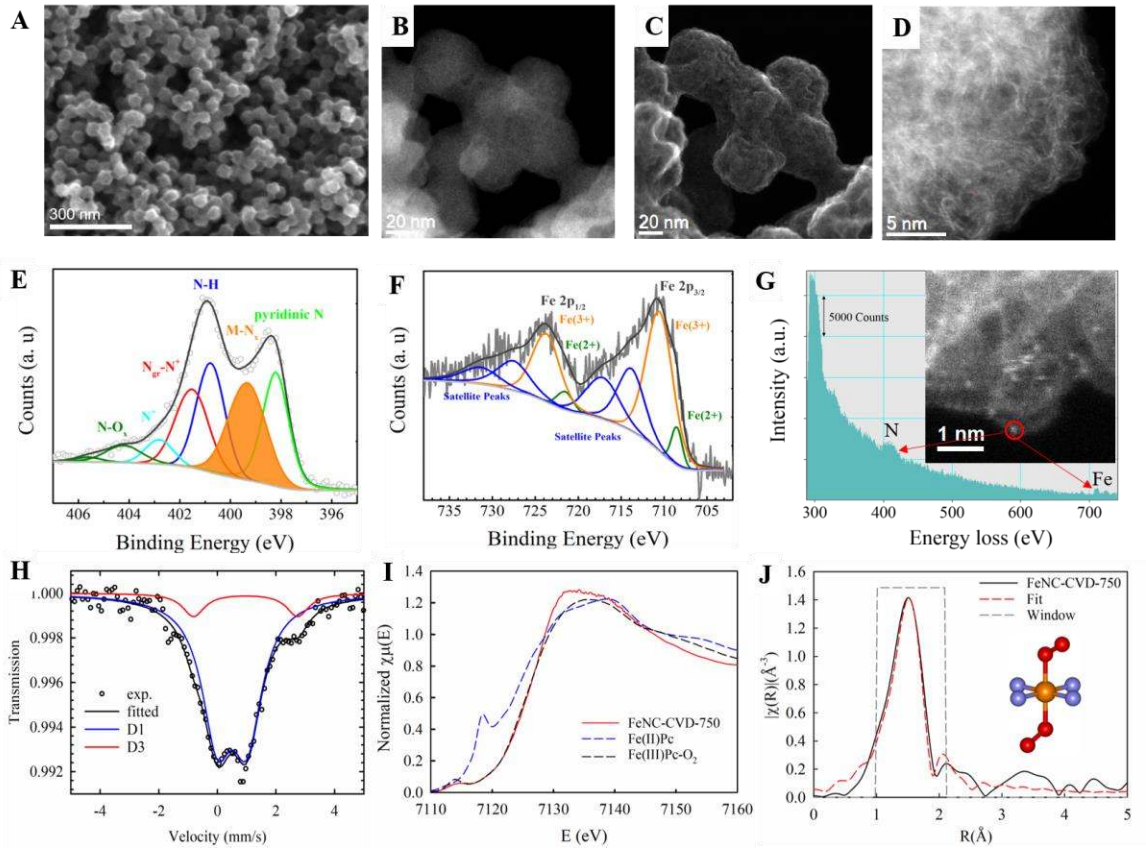

Figure 3. **Characterizations of FeNC-CVD-750**. (**A**) SEM image and (**B**) ADF- and (**C**) SE-STEM image pair and (**D**) atomic-resolution ADF-STEM image. (**E**) High-resolution N_{1s} XPS spectrum. The assignments of N species follow the recent work (*24*). (**F**) High-resolution XPS Fe_{2p} spectrum fitted with Fe(III) (90%) and Fe(II) (10%) species. (**G**) EEL spectrum showing N K-edge and Fe L-edge acquired from single atom (bright dot in the inset in which an atomic-resolution AC-STEM image is displayed). (**H**) Mössbauer spectrum measured at 5 K fitted with D1 (89%) and D3 (11%). (**I**) *Ex situ* XANES spectrum together with those of Fe(II)Pc and Fe(III)Pc-O_2 standards for comparison. (**J**) *Ex situ* FT-EXAFS spectrum and the fit with the model of O_2-Fe(III)-N_4 present in the inset wherein the orange, red, and purple balls represent Fe, O, and N atoms, respectively.

The presence of Fe-N_4 moieties in FeNC-CVD-750 is also supported by the ^{57}Fe Mössbauer spectrum collected at 5 Kelvin (Figure 3H). The lowest possible temperature during Mössbauer data acquisition is important to distinguish superparamagnetic Fe species (such as nano-Fe-oxides) from Fe-N_4 sites. While both nano-Fe-oxides and O_2-Fe(III)-N_4 sites lead to a similar D1 signal at room temperature, this degeneracy is

usually unveiled at 5 K: nanosized superparamagnetic Fe oxides convert into a sextet component while O_2-Fe(III)-N_4 sites still contribute with a D1 component (*35*).

The ^{57}Fe Mössbauer spectrum at 5K of FeNC-CVD-750 identifies two doublets, labelled D1 and D3, representing 89% and 11% of the absorption area, respectively (Figure 3H and Table S3). D1 has been commonly observed for Fe-N-C materials and has recently been assigned to O_2-Fe(III)-N_4 (*14, 17, 18*). D3 can be unambiguously assigned to a high spin Fe^{2+} species, due to its high IS of 0.97 mm/s. A doublet with similar isomer shift (IS) and quadrupole slitting (QS) than those of D3 here were usually observed in Fe-N-C catalysts synthesized using iron chlorides as the Fe precursors (*17, 36*). Due to this observation and the match of IS and QS values of D3 with those of $FeCl_2$ (*37*), and even closer match with $FeCl_2$-graphite intercalation compounds (*38*), we assign the D3 component in FeNC-CVD-750 to $FeCl_2$. This assignment quantitatively agree with the XPS results of ~90% Fe(III) and ~10% Fe(II), and together leads to U_{Fe} = ~90% and U_{FeN4} = 100%, and an overall high Fe utilization (U) of ~90%, according to Eq. 2. To further prove this, we determined the electrochemically active Fe content in the FeNC-CVD-750 RDE electrode from the area of the redox peak around 0.66 V, shown in Figure 4A. These redox peaks, which are absent in the *CV* of the N-C, have been previously assigned to the Fe(III)/Fe(II) redox transition of Fe-N_4 sites in H_2SO_4 solution (*39*). The electroactive Fe content on the RDE electrode is found to be 14.7 $\mu g \cdot cm^{-2}$. Given the catalyst loading of 800 $\mu g \cdot cm^{-2}$ and an Fe content of 2.0 wt% for FeNC-CVD-750 (Table S2), the overall utilization (U) of FeNC-CVD-750 is found to be 92% (Eq. S3). This value agrees well with the U of ~90% derived from spectroscopic analysis and the

aforementioned assignments of D1 to air-accessible Fe-N_4 sites and D3 to $FeCl_2$, thereby confirming the full utilization of Fe-N_4 sites in FeNC-CVD-750 (U_{FeN4} = 100%).

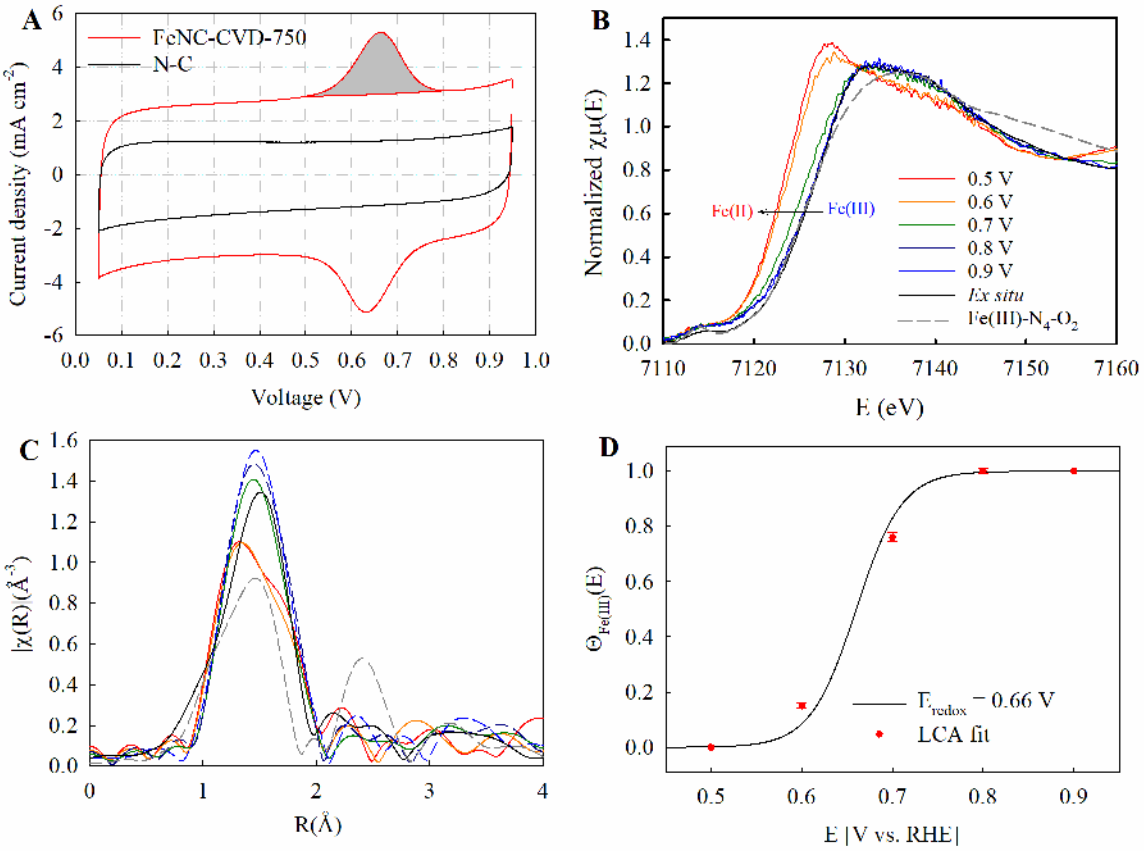

Figure. 4. ***In situ*** **characterization of FeNC-CVD-750**. (**A**) Cyclic voltammograms (*CVs*) of the FeNC-CVD-750 and N-C collected in Ar-saturated 0.5 M H_2SO_4 electrolyte at room temperature with a scan rate of 10 mV·s^{-1}. (**B**) *In situ* XANES and (**C**) FT-EXAFS of FeNC-CVD-750 collected in O_2-purged 0.5 M H_2SO_4 at room temperature as a function of potential during the anodic-going scan. (**D**) Comparison of the fraction of Fe(III) over the total amounts of Fe ($\Theta_{Fe(III)}$) as a function of potential derived from the linear combination analysis (LCA) of the XANES spectra (red dots) and from Eq. 3 with a redox potential (E_{redox}) of 0.66 V.

To further confirm that all the Fe-N_4 sites in FeNC-CVD-750 are electrochemically active during the ORR, we conducted *in situ* XAS on FeNC-CVD-750 at the Fe K-edge in an O_2-purged 0.5 M H_2SO_4 electrolyte in a flow cell (*40*) as a function of applied potential. The XANES and FT-EXAFS spectra collected at 0.9 V nearly overlap that of Fe(III)Pc-O_2 (Figure 4B), which confirms that the vast majority of Fe-N_4 sites are in the

form of Fe(III)-N_4-O_2 at 0.9 V (Table S4). As the potential is gradually reduced to 0.5 V, the XANES spectrum shifts negatively, and correspondingly the intensity of the FT-EXAFS peak drops (Figure 4C). These occurrences have been commonly observed on Fe-N-C catalysts and ascribed to the redox transition from Fe(III)-N_4-O_2 to Fe(II)-N_4 (*6, 14, 30, 31*). However, the FT-EXAFS spectrum at 0.5 V exhibits a shoulder around 1.8 Å, rather than just the one prominent peak observed at 0.9 V (Figure 4C), and it cannot be fitted with an Fe-N_4 model. A recent *in situ* Mössbauer and XAS study in H_2SO_4 solution proposed that as the potential is decreased, the Fe(III)-N_4-O_2 moiety is converted to Fe(II)-N_4 with an axial bond with a sulfate ion, Fe(II)-N_4-SO_4 (*41*). We accordingly assign the Fe species at 0.5 V to Fe(II)-N_4-SO_4. The conversion of one Fe species to another with changing potential applied to FeNC-CVD-750 is further confirmed by the existence of isobestic points at 7132 and 7154 eV in the XANES spectra (Figure 4B). By taking the XANES spectra at 0.9 V and 0.5 V as standards representing Fe(III)-N_4-O_2 and Fe(II)-N_4-SO_4, respectively, the fraction of Fe(III) ($\Theta_{Fe(III)}(E)$ = Fe(III)/(Fe(III)+Fe(II)); E represents the applied potential) can be acquired by linear combination analysis (LCA) of the *in situ* XANES spectra. As seen in Figure 3D, the $\Theta_{Fe(III)}(E)$ acquired by the LCA closely follows the one calculated from the equation (*42*):

$$\Theta_{\mathrm{Fe(III)}}(\mathrm{E}) = \frac{1}{1+\mathrm{e}^{\frac{-\mathrm{F}}{\mathrm{RT}}(\mathrm{E}-E_{redox})}} \qquad (3)$$

where *F* is the Faraday constant, *R* is the universal gas constant, *T* is the temperature, and E_{redox} is the Fe(II)/Fe(III) redox potential derived from the redox peaks in the *CV* of FeNC-CVD-750 in deaerated electrolyte (Figure 4A), 0.66 V. These *in situ* XAS results thus corroborate full utilization of Fe-N_4 sites in FeNC-CVD-750 during the ORR.

The simultaneous achievements of U_{FeN4} =100% and U_{Fe} = ~90% leads to an ultrahigh *U* of ~90% on FeNC-CVD-750 that meanwhile possesses a relatively high Fe content of 2 wt%. This *U* is six times higher than that (14.1%) of a state-of-the-art Fe-N-C catalyst with comparable bulk Fe content (2.14 wt%) (*12*). This indicates that the negative correlation between the Fe wt% and *U* in traditional Fe-N-C catalysts has been substantially alleviated in FeNC-CVD-750 using the CVD method. Consequently, the FeNC-CVD-750 catalyst has a record-high SD_{mass} of 2×10^{20} sites·g^{-1} (Eq. S2), which is more than three times higher than the values reported thus far for Fe-N-C catalysts (*12, 20, 43*) and approaching the SD_{mass} of 47% Pt/C (3.2×10^{20} sites·g^{-1}) (*22*). The TOF of the Fe-N_4 sites in FeNC-CVD-750 at 0.8 V is 0.78 $e^{-}\cdot site^{-1}\cdot s^{-1}$, as derived from the kinetic current density at 0.8 V and SD_{mass} (Eq. S4). This value is comparable to those of previous Fe-N-C catalysts (*41, 44*), but one order of magnitude lower than that of Pt/C (*21, 22*). Therefore, the ultra-high kinetic current density of FeNC-CVD-750 is mainly ascribed to the record-high SD_{mass} achieved by CVD, not to a record-high TOF compared to previous state-of-art Fe-N-C catalysts.

The high SD_{mass} of FeNC-CVD-750 is necessary for its high performance in an MEA. In addition, the ADF-STEM images of the cathode of the MEA show the preservation of the particle morphology of FeNC-CVD-750 without noticeable agglomeration (Figure 5A and Figure S6). The corresponding overlaid EDS images show relatively uniform distribution of Fe atoms in the electrode and fluorine from the ionomer distributed over the surface of the carbon particles, suggesting these two elements are located in close proximity to one another (Figure 5B-D). These results indicate that the Fe-N_4 sites in the cathode are readily accessible to protons. The preservation of the particle morphology of

FeNC-CVD-750 in an MEA and the high accessibility of Fe-N_4 sites to protons and O_2 indicate that its high SD_{mass} can be utilized efficiently, accounting for the exceptional ORR performance of FeNC-CVD-750 in a PEMFC, at both low and high current densities.

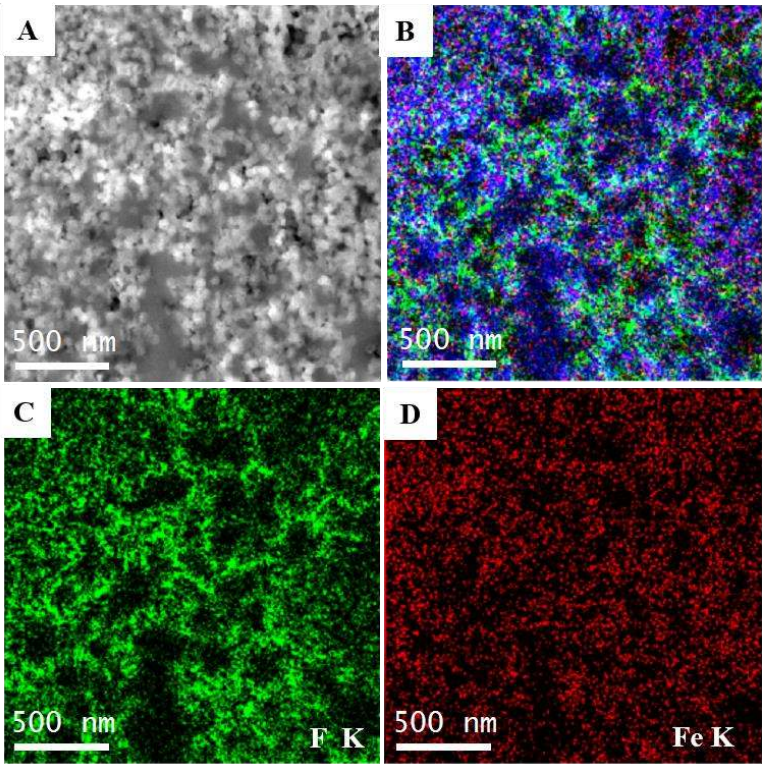

Figure 5. **Imaging FeNC-CVD-750 electrode**. (**A**) ADF-STEM image of the cathode of the MEA with (**B-D**) corresponding energy dispersive X-ray spectroscopy (EDS) spectrum images. The blue, red, and green colors represent the C, Fe, and F from the ionomer, respectively.

The mechanism of the formation of Fe-N_4 sites by CVD. Next, we show that the CVD approach leads to a different Fe-N_4 site formation mechanism from the previous synthetic approaches. The background *CV* of FeNC-CVD-750 is much broader than that of N-C, in addition to the emergence of the Fe(III)/Fe(II) redox peaks (Figure 3D). The double-layer capacitance of the N-C derived from the *CV* at 0.3 V is ~0.16 F·mg^{-1}. Assuming a

specific capacitance of the carbon surface of 204 $mF \cdot m^{-2}$ (*14*), this corresponds to an electrochemical surface area (ECSA) of ~812 $m^2 \cdot g^{-1}$. This value matches its BET area of 807 $m^2 \cdot g^{-1}$. After the CVD at 750 °C, the double-layer capacitance markedly increases to ~0.36 $F \cdot mg^{-1}$, corresponding to a high ECSA of ~1800 $m^2 \cdot g^{-1}$, close to the BET area of ~1593 $m^2 \cdot g^{-1}$ of FeNC-CVD-750. The differential pore distribution analysis shows a substantial increase in the abundance of both micropores (< 2 nm) and mesopores (Figure S7) after the CVD.

The dramatic enhancement of the ECSA of the N-C after the CVD at 750 °C does not occur when the CVD is performed at 650 °C. The *CV* of FeNC-CVD-650 is only slightly broader than that of the N-C (Figure S8). In addition, the SD_{mass} of FeNC-CVD-650 derived from the redox peak area (Figure S8) is 5×10^{19} sites$\cdot g^{-1}$, much lower than that of FeNC-CVD-750. Meanwhile, the Zn content in FeNC-CVD-650 remains high at ~1.05 wt% (Table S2), much higher than that (0.12 wt%) observed in FeNC-CVD-750. This comparison suggests that the enhancement of the porosity of N-C and the formation of Fe-N_4 sites are closely related to the removal of Zn. The substantial loss of Zn upon CVD at 750 °C is not caused by the evaporation of metallic Zn since 750 °C is much lower than the boiling point of Zn (907 °C). Zn evaporation started only above 850 °C in previous syntheses of ZIF-8-derived Fe-N-C catalysts (*7, 9*). We note that (1) $ZnCl_2$ has a lower boiling point of 732 °C, (2) Zn is nearly completely removed after CVD at 750 °C but not at 650 °C, (3) the removal of 2.16 wt% Zn is accompanied by an increase of Fe content by a comparable amount, 2.00 wt% (Table S2), without changing the metal-N XPS peak significantly (Figure S4B), and (4) both the Zn in the N-C and the Fe in the FeNC-CVD-750 are in the form of M-N_4. These combined results lead us to propose that the Fe-N_4

sites are formed via the following displacement reaction during the CVD at 750 °C (Scheme 1A):

$$2\ FeCl_3\ (g) + 2\ Zn\text{-}N_4 \rightarrow 2\ Fe\text{-}N_4 + 2\ ZnCl_2\ (g) + Cl_2\ (g) \quad (4)$$

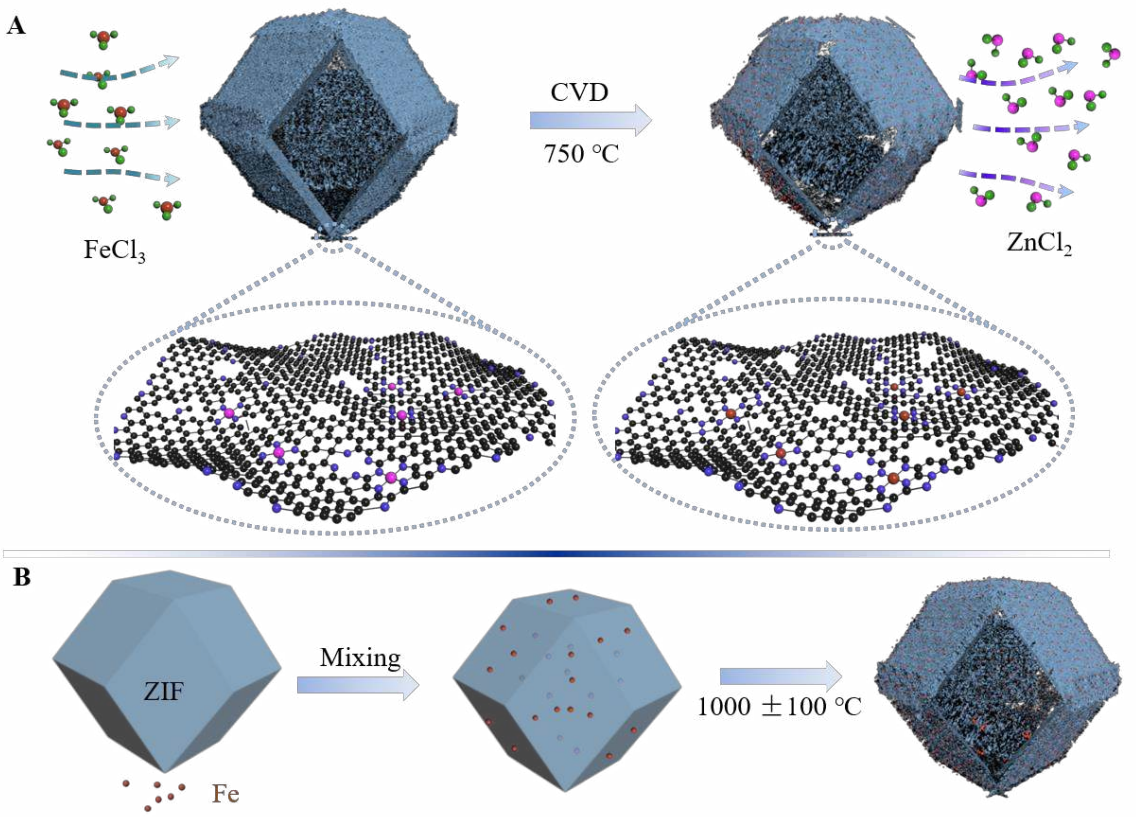

Scheme 1. **Fe-N-C synthesis approaches**. (A) Synthesis of FeNC-CVD-750 via CVD. (B) The currently established major approach for the synthesis of Fe-N-C catalysts.

According to this $Fe\text{-}N_4$ formation mechanism, the penetration of the iron chloride vapor into the N-C plus release of $ZnCl_2$ vapor are responsible for the dramatic enhancement in porosity or ECSA upon the CVD at 750 °C. This notion also rationalizes the optimized temperature of 750 °C for the CVD method. A temperature of 750 °C is marginally higher than the boiling point of $ZnCl_2$ (732 °C), so the $ZnCl_2$ is readily released in the vapor form, thereby promoting the displacement reaction (Eq. 4), forming $Fe\text{-}N_4$.

Meanwhile, The Fe-N_4 sites are more thermally stable at 750 °C than at higher temperature. This is reflected by the observation that the N content in FeNC-CVD-750 is highly comparable to that of the N-C, but drops precipitously at higher temperatures (Table S2). The rapid drop of the N content in Fe-N-C catalysts with increasing pyrolysis temperature has been commonly observed and regarded as one key factor limiting the Fe-N_4 site density (*7, 9*). Therefore, the Fe-N_4 sites are better preserved in the synthesis of FeNC-CVD-750 at a temperature approximately 200 °C lower than that (1000±100 °C) utilized for the synthesis of previous state-of-the-art Fe-N-C catalysts.

The displacement reaction (Eq. 4) also accounts for the full utilization of Fe-N_4 sites in FeNC-CVD-750. With this mechanism, the Fe-N_4 sites are formed at the locations where the Zn-N_4 sites are accessible by iron chloride vapor, and thus accessible by air. In addition, the release of $ZnCl_2$ vapor from the formed Fe-N_4 sites may further improve their accessibility. In contrast, previous synthesis methods extensively mix Fe, N, and C precursors prior to pyrolysis (Scheme 1B). Consequently, the Fe-N_4 moieties are distributed throughout the carbon matrix, whereas only those in the outer-surface region are accessible by air. These Fe-N-C catalysts show both the D1 and D2 spectroscopic signatures in their ^{57}Fe Mössbauer spectra, in comparable amounts, with D2 recently assigned to Fe(II)-N_4 moieties free of adsorbed oxygenated species atop the ferrous central cation (*18*). These assignments strongly suggest that the D2 signature corresponds to Fe-N_4 sites located in the bulk. For example, D2 accounted for 49% and 62% of the relative absorption area of Mössbauer spectra of the ICL and UNM catalysts, the two benchmark Fe-N-C catalysts with the highest U_{FeN4} values (*20*). Hence, the current state-of-art Fe-N-C catalysts have a U_{FeN4} significantly lower than 100%. Therefore, although

full utilization of active sites has long been conceived as a unique advantage of single-atom catalysts, this is the first time it has been realized in Fe-N-C catalysts by resorting to a dual-step synthesis and CVD deposition of Fe.

Collectively, CVD (at 750 °C) possesses two essential advantages compared to previous synthesis approaches for Fe-N-C catalysts: (1) the Fe-N_4 sites are formed at a much lower temperature (allowing increased N-content and therefore increased Fe-N_4 sites, as well as mitigated Fe clustering) and (2) the Fe-N_4 sites are located on the outer-surface of the material with full site utilization ($U_{FeN4} = 100\%$). Consequently, the FeNC-CVD-750 catalyst possesses a record-high SD_{mass} and ORR performance in H_2-O_2 PEMFCs. It is also a model catalyst containing only one type of active site. Therefore, model catalyst and practical catalyst for the ORR are combined in a single entity by using the CVD approach. The CVD approach pioneered here is widely applicable to the synthesis of single-atom catalysts with other metals (Mn, Co) and other substrates (metal oxides) for many applications.

ACKNOWLEDGEMENTS

This work was supported by the US Department of Energy under award number DE-EE0008416 and DE-EE0008075. The authors acknowledge the support from the U.S. Department of Energy, Energy Efficiency and Renewable Energy, Hydrogen and Fuel Cell Technologies Office (DOE-EERE-HFTO) through the Electrocatalysis consortium (ElectroCat) and the DOE program and technology managers, Dimitrios Papageorgopoulos, David Peterson, and Nancy Garland. The *ex situ* XAS experiments at the Zn K-edge were performed at the Advanced Photon Source (APS), a DOE Office of

Science User Facility operated for the DOE Office of Science by Argonne National Laboratory under Contract No. DE-AC02-06CH11357. The operation of MRCAT at the APS is supported by the Department of Energy and the MRCAT member institutions. The rest of the XAS data were collected at the beamlines 6-BM, 7-BM and 8-ID (ISS) of the National Synchrotron Light Source II, a U.S. Department of Energy (DOE) Office of Science User Facility operated for the DOE Office of Science by Brookhaven National Laboratory under Contract No. DE-SC0012704. AC-STEM was conducted at the Center for Nanophase Materials Sciences located at Oak Ridge National Laboratory, which is a DOE Office of Science User Facility.

COMPETING INTERESTS

L.J., S.M., and Q.J. have filed a provisional patent (NO. 62/945,861) application based on the results of this manuscript.

AUTHOR CONTRIBUTIONS

Q.J., D.J.M., and F.J. conceived the project. Q.J. and J.L. conceived and designed the CVD method. Q.J., J.L., D.J.M., F.J, and L.J. developed the CVD method. L.J. synthesized the FeNC-CVD-T catalysts; Q.J. and S.M. supervised and advised the synthesis. L.J. conducted the RDE, BET, XRD, TEM, SEM, and ICP-OES. L.J., Q.S., L.L.R., T.S., E.L., and Q.J. conducted the XAS on the FeNC-CVD-750. T.S. and D.J.M. conducted the XAS on the N-C and ZIF-8 at the Zn K-edge. Q.J. analyzed the XAS data. M.S., J.L., and F.J. conducted the Mössbauer and the fitting. Z.Z. and Y.H. conducted the XPS and fitting. F.Y., S.Z., and H.X. conducted the PEMFC operation and data analysis.

D.A.C. conducted the ADF-STEM, EELS, and data analysis. Q.J., F.J., D.J.M., and L.J. wrote the manuscript and prepared the figures.

SUPPLEMENTARY MATERIALS

Materials and Methods
Figs. S1 to S8
Tables S1 to S4
Equation S1 to S4
References (45-47)

REFERENCES AND NOTES

1. T. Yoshida, K. Kojima, Toyota MIRAI fuel cell vehicle and progress toward a future hydrogen society. *Electrochem Soc Interface* **24**, 45-49 (2015).
2. S. T. Thompson, B. D. James, J. M. Huya-Kouadio, C. Houchins, D. A. DeSantis, R. Ahluwalia, A. R. Wilson, G. Kleen, D. Papageorgopoulos, Direct hydrogen fuel cell electric vehicle cost analysis: system and high-volume manufacturing description, validation, and outlook. *J. Power Sources* **399**, 304-313 (2018).
3. S. T. Thompson, A. R. Wilson, P. Zelenay, D. J. Myers, K. L. More, K. C. Neyerlin, D. Papageorgopoulos, ElectroCat: DOE's approach to PGM-free catalyst and electrode R&D. *Solid State Ion.* **319**, 68-76 (2018).
4. H. T. Chung, D. A. Cullen, D. Higgins, B. T. Sneed, E. F. Holby, K. L. More, P. Zelenay, Direct atomic-level insight into the active sites of a high-performance PGM-free ORR catalyst. *Science* **357**, 479-484 (2017).
5. J. Li, M. Chen, D. A. Cullen, S. Hwang, M. Wang, B. Li, K. Liu, S. Karakalos, M. Lucero, H. Zhang, C. Lei, H. Xu, G. E. Sterbinsky, Z. Feng, D. Su, K. L. More, G. Wang, Z. Wang, G. Wu, Atomically dispersed manganese catalysts for oxygen reduction in proton-exchange membrane fuel cells. *Nat. Catal.* **1**, 935-945 (2018).

6. A. Zitolo, N. Ranjbar-Sahraie, T. Mineva, J. Li, Q. Jia, S. Stamatin, G. F. Harrington, S. M. Lyth, P. Krtil, S. Mukerjee, E. Fonda, F. Jaouen, Identification of catalytic sites in cobalt-nitrogen-carbon materials for the oxygen reduction reaction. *Nat. Commun.* **8**, 957 (2017).

7. H. Zhang, S. Hwang, M. Wang, Z. Feng, S. Karakalos, L. Luo, Z. Qiao, X. Xie, C. Wang, D. Su, Y. Shao, G. Wu, Single atomic iron catalysts for oxygen reduction in acidic media: particle size control and thermal activation. *J. Am. Chem. Soc.* **139**, 14143-14149 (2017).

8. M. Lefèvre, E. Proietti, F. Jaouen, J.-P. Dodelet, Iron-based catalysts with improved oxygen reduction activity in polymer electrolyte fuel cells. *Science* **324**, 71-74 (2009).

9. E. Proietti, F. Jaouen, M. Lefèvre, N. Larouche, J. Tian, J. Herranz, J.-P. Dodelet, Iron-based cathode catalyst with enhanced power density in polymer electrolyte membrane fuel cells. *Nat. Commun.* **2**, 416 (2011).

10. D. Banham, T. Kishimoto, Y. Zhou, T. Sato, K. Bai, J.-i. Ozaki, Y. Imashiro, S. Ye, Critical advancements in achieving high power and stable nonprecious metal catalyst–based MEAs for real-world proton exchange membrane fuel cell applications. *Sci. Adv.* **4**, 7180 (2018).

11. A. Serov, K. Artyushkova, E. Niangar, C. Wang, N. Dale, F. Jaouen, M.-T. Sougrati, Q. Jia, S. Mukerjee, P. Atanassov, Nano-structured non-platinum catalysts for automotive fuel cell application. *Nano Energy* **16**, 293-300 (2015).

12. X. Wan, X. Liu, Y. Li, R. Yu, L. Zheng, W. Yan, H. Wang, M. Xu, J. Shui, Fe–N–C electrocatalyst with dense active sites and efficient mass transport for high-performance proton exchange membrane fuel cells. *Nat. Catal.* **2**, 259-268 (2019).

13. U. Tylus, Q. Jia, K. Strickland, N. Ramaswamy, A. Serov, P. Atanassov, S. Mukerjee, Elucidating oxygen reduction active sites in pyrolyzed metal–nitrogen coordinated non-precious-metal electrocatalyst systems. *J. Phys. Chem. C* **118**, 8999-9008 (2014).
14. J. Li, S. Ghoshal, W. Liang, M.-T. Sougrati, F. Jaouen, B. Halevi, S. McKinney, G. McCool, C. Ma, X. Yuan, Z.-F. Ma, S. Mukerjee, Q. Jia, Structural and mechanistic basis for the high activity of Fe-N-C catalysts toward oxygen reduction. *Energy Environ. Sci.* **9**, 2418-2432 (2016).
15. H. Zhang, H. T. Chung, D. A. Cullen, S. Wagner, U. I. Kramm, K. L. More, P. Zelenay, G. Wu, High-performance fuel cell cathodes exclusively containing atomically dispersed iron active sites. *Energy Environ. Sci.* **12**, 2548-2558 (2019).
16. S. Gupta, D. Tryk, I. Bae, W. Aldred, E. Yeager, Heat-treated polyacrylonitrile-based catalysts for oxygen electroreduction. *J. Appl. Electrochem.* **19**, 19-27 (1989).
17. J. Li, L. Jiao, E. Wegener, L. L. Richard, E. Liu, A. Zitolo, M. T. Sougrati, S. Mukerjee, Z. Zhao, Y. Huang, F. Yang, S. Zhong, H. Xu, A. J. Kropf, F. Jaouen, D. J. Myers, Q. Jia, Evolution pathway from iron compounds to $Fe_1(II)–N_4$ sites through gas-phase iron during pyrolysis. *J. Am. Chem. Soc.* **142**, 1417-1423 (2020).
18. T. Mineva, I. Matanovic, P. Atanassov, M.-T. Sougrati, L. Stievano, M. Clémancey, A. Kochem, J.-M. Latour, F. Jaouen, Understanding active sites in pyrolyzed Fe–N–C catalysts for fuel cell cathodes by bridging density functional theory calculations and ^{57}Fe mössbauer spectroscopy. *ACS Catal.* **9**, 9359-9371 (2019).
19. A. Zitolo, V. Goellner, V. Armel, M.-T. Sougrati, T. Mineva, L. Stievano, E. Fonda, F. Jaouen, Identification of catalytic sites for oxygen reduction in iron- and nitrogen-doped graphene materials. *Nat. Mater.* **14**, 937 (2015).

20. Primbs, M.; Sun, Y.; Roy, A.; Malko, D.; Mehmood, A.; Sougrati, M.-T.; Blanchard, P.-Y.; Granozzi, G.; Kosmala, T.; Daniel, G.; Atanassov, P.; Sharman, J.; Durante, C.; Kucernak, A.; Jones, D.; Jaouen, F.; Strasser, P. Establishing reactivity descriptors for platinum group metal (PGM)-free Fe–N–C catalysts for PEM fuel cells. *Energy Environ. Sci.* **2020**, *13*, 2480-2500.

21. U. A. Paulus, A. Wokaun, G. G. Scherer, T. J. Schmidt, V. Stamenkovic, N. M. Markovic, P. N. Ross, Oxygen reduction on high surface area Pt-based alloy catalysts in comparison to well defined smooth bulk alloy electrodes. *Electrochim. Acta* **47**, 3787-3798 (2002).

22. H. A. Gasteiger, S. S. Kocha, B. Sompalli, F. T. Wagner, Activity benchmarks and requirements for Pt, Pt-alloy, and non-Pt oxygen reduction catalysts for PEMFCs. *Appl. Catal. B-Environ.* **56**, 9-35 (2005).

23. F. Luo, A. Roy, L. Silvioli, D. A. Cullen, A. Zitolo, M. T. Sougrati, I. C. Oguz, T. Mineva, D. Teschner, S. Wagner, J. Wen, F. Dionigi, U. I. Kramm, J. Rossmeisl, F. Jaouen, P. Strasser, P-block single-metal-site tin/nitrogen-doped carbon fuel cell cathode catalyst for oxygen reduction reaction. *Nat. Mater.*, (2020). doi.org/10.1038/s41563-020-0717-5

24. K. Artyushkova, Misconceptions in interpretation of nitrogen chemistry from x-ray photoelectron spectra. *J. Vac. Sci. Technol. A* **38**, 031002 (2020).

25. *See supplementary materials.*

26. J. Li, P. Pršlja, T. Shinagawa, A. J. Martín Fernández, F. Krumeich, K. Artyushkova, P. Atanassov, A. Zitolo, Y. Zhou, R. García-Muelas, N. López, J. Pérez-Ramírez, F.

Jaouen, Volcano trend in electrocatalytic CO_2 reduction activity over atomically dispersed metal sites on nitrogen-doped carbon. *ACS Catal.* **9**, 10426-10439 (2019).

27. N. Kanari, D. Mishra, L. Filippov, F. Diot, J. Mochón, E. Allain, Kinetics of hematite chlorination with Cl_2 and Cl_2+O_2: Part I. Chlorination with Cl_2. *Thermochim. Acta* **497**, 52-59 (2010).
28. D. S. Rustad, N. W. Gregory, Vapor pressure of iron(III) chloride. *J. Chem. Eng.* **28**, 151-155 (1983).
29. D. E. Beltrán, S. Litster, Half-wave potential or mass activity? characterizing platinum group metal-free fuel cell catalysts by rotating disk electrodes. *ACS Energy Lett.* **4**, 1158-1161 (2019).
30. L. Osmieri, R. K. Ahluwalia, X. Wang, H. T. Chung, X. Yin, A. J. Kropf, J. Park, D. A. Cullen, K. L. More, P. Zelenay, D. J. Myers, K. C. Neyerlin, Elucidation of Fe-N-C electrocatalyst active site functionality via in-situ X-ray absorption and operando determination of oxygen reduction reaction kinetics in a PEFC. *Appl. Catal. B-Environ.* **257**, 117929 (2019).
31. J. Li, A. Alsudairi, Z.-F. Ma, S. Mukerjee, Q. Jia, Asymmetric volcano trend in oxygen reduction activity of Pt and non-Pt catalysts: *in situ* identification of the site-blocking effect. *J. Am. Chem. Soc.* **139**, 1384-1387 (2017).
32. Y. Shao, J.-P. Dodelet, G. Wu, P. Zelenay, PGM-free cathode catalysts for PEM fuel cells: a mini-review on stability challenges. *Adv. Mater.* **31**, 1807615 (2019).
33. L. Osmieri, D. A. Cullen, H. T. Chung, R. K. Ahluwalia, K. C. Neyerlin, Durability evaluation of a Fe–N–C catalyst in polymer electrolyte fuel cell environment via accelerated stress tests. *Nano Energy* **78**, 105209 (2020).

34. L. Osmieri, J. Park, D. A. Cullen, P. Zelenay, D. J. Myers, K. C. Neyerlin, Status and Challenges for the application of platinum group metal-free catalysts in proton exchange membrane fuel cells. *Current Opinion in Electrochemistry*, (2020). DOI: 10.1016/j.coelec.2020.08.009

35. J. Li, Q. Jia, S. Mukerjee, M.-T. Sougrati, G. Drazic, A. Zitolo, F. Jaouen, The challenge of achieving a high density of Fe-based active sites in a highly graphitic carbon matrix. *Catalysts* **9**, 144 (2019).

36. D. Menga, F. Ruiz-Zepeda, L. Moriau, M. Šala, F. Wagner, B. Koyutürk, M. Bele, U. Petek, N. Hodnik, M. Gaberšček, T.-P. Fellinger, Active-site imprinting: preparation of Fe–N–C catalysts from zinc ion–templated ionothermal nitrogen-doped carbons. *Adv. Energy Mater.* **9**, 1902412 (2019).

37. T. Birchall, An investigation of some iron halide complexes by Mössbauer spectroscopy. *Can. J. Chem.* **47**, 1351-1354 (1969).

38. Z. D. Wang, M. Inagaki, M. takano, Moessbauer study of iron chloride-graphite intercalation compounds synthesized in molten salt. *Carbon* **29**, 423-427 (1991).

39. G. Wu, K. L. More, C. M. Johnston, P. Zelenay, High-performance electrocatalysts for oxygen reduction derived from polyaniline, iron, and cobalt. *Science* **332**, 443-447 (2011).

40. T. M. Arruda, B. Shyam, J. S. Lawton, N. Ramaswamy, D. E. Budil, D. E. Ramaker, S. Mukerjee, Fundamental aspects of spontaneous cathodic deposition of Ru onto Pt/c electrocatalysts and membranes under direct methanol fuel cell operating conditions: an *in situ* X-ray absorption spectroscopy and electron spin resonance study. *J. Phys. Chem. C* **114**, 1028-1040 (2010).

41. P. Zelenay and D.J. Myers, "ElectroCat (Electrocatalysis Consortium)", 2020 Department of Energy Hydrogen and Fuel Cells Program 2020 Annual Merit Review and Peer Evaluation Meeting, Washington D. C., 2020. (https://www.hydrogen.energy.gov/pdfs/review20/fc160_myers_zelenay_2020_o.pdf)
42. S. Gottesfeld, Generation of active sites by potential-driven surface processes: a central aspect of electrocatalysis. *ECS Trans* **61**, 1-13 (2014).
43. F. Luo, C. H. Choi, M. J. M. Primbs, W. Ju, S. Li, N. D. Leonard, A. Thomas, F. Jaouen, P. Strasser, Accurate evaluation of active-site density (SD) and turnover frequency (TOF) of PGM-free metal–nitrogen-doped carbon (MNC) electrocatalysts using CO cryo adsorption. *ACS Catal.* **9**, 4841-4852 (2019).
44. U. I. Kramm, J. Herranz, N. Larouche, T. M. Arruda, M. Lefèvre, F. Jaouen, P. Bogdanoff, S. Fiechter, I. Abs-Wurmbach, S. Mukerjee, J.-P. Dodelet, Structure of the catalytic sites in Fe/N/C-catalysts for O_2-reduction in PEM fuel cells. *Phys. Chem. Chem. Phys.* **14**, 11673-11688 (2012).

Supporting Information of

Chemical vapor deposition of Fe-N-C oxygen reduction catalysts with full utilization of dense Fe-N_4 sites

Li Jiao[1], Jingkun Li[2], Lynne LaRochelle Richard[3], Qiang Sun[3], Thomas Stracensky[3], Ershuai Liu[3], Moulay Tahar Sougrati[2], Zipeng Zhao[4], Fan Yang[5], Sichen Zhong[5], Hui Xu[5], Sanjeev Mukerjee[3], Yu Huang[4,6], David A. Cullen[7], Deborah J. Myers*[,8], Frédéric Jaouen*[,2], and Qingying Jia*[,3]

[1]Department of Chemical Engineering, Northeastern University, Boston, Massachusetts, 02115, United States

[2]Institut Charles Gerhardt Montpellier, UMR 5253, CNRS, Université Montpellier, ENSCM, Place Eugène Bataillon, 34095 Montpellier cedex 5, France

[3]Department of Chemistry and Chemical Biology, Northeastern University, Boston, Massachusetts, 02115, United States

[4]Department of Materials Science and Engineering, University of California, Los Angeles, California, 90095, United States

[5]Giner, Inc, Newton, Massachusetts, 02466, United States.

[6]California NanoSystems Institute (CNSI), University of California, Los Angeles, California, 90095

[7]Center for Nanophase Materials Sciences, Oak Ridge National Laboratory, Oak Ridge, Tennessee 37831, USA

[8]Chemical Sciences and Engineering Division, Argonne National Laboratory, Lemont, Illinois, 60439, United States

*Correspondence authors. Emails: dmyers@anl.gov (D. M.); frederic.jaouen@umontpellier.fr (F. J.); q.jia@northeastern.edu (Q. J.)

Materials and Methods

Chemicals: Zinc nitrate hexahydrate ($Zn(NO_3)_2 \cdot 6H_2O$, ≥ 99.0%), 2-methylimidazole (99%), methanol solution, zinc phthalocyanine (Zn(II)Pc, 97%), 1,10-phenanthroline monohydrate, ethanol solution, anhydrous Iron(III) chloride ($FeCl_3$, 99%), iron(II) phthalocyanine (Fe(II)Pc, 95%), Iron(III) phthalocyanine-tetrasulfonic acid (Fe(III)Pc-O_2, 80%), and sulfuric acid (H_2SO_4, 95-97%, PPT Grade) were all purchased from Sigma-Aldrich. All aqueous solutions were prepared using deionized (DI) water (18.2 MΩ·cm) obtained from an ultra-pure purification system (Aqua Solutions).

Synthesis of zeolitic imidazolate framework eight (ZIF-8). 200 ml homogeneous 0.1 M $Zn(NO_3)_2 \cdot 6H_2O$ methanol solution was added to 200 ml 0.4 M 2-methylimidazole methanol solution under magnetic stirring for one hour at room temperature. The suspension was collected and washed by centrifugation using methanol three times, and then dried at 40 ^oC in a vacuum oven overnight.

Synthesis of N-C: 1.0 g ZIF-8 and 0.25 g 1,10 phenanthroline were dispersed in a solution of ethanol and deionized water with a volume ratio of 2:1. The mixture was magnetically stirred for two hours and then dried at 80 ^oC in a vacuum oven overnight. The dry powders were ball milled for 3 hours in a plastic container with 5 plastic balls with a diameter of 0.25 inch. The collected powders were pyrolyzed under Ar at 1050 ℃ for one hour after reaching 1050 ℃ with a ramping rate of 5 ^oC per minute, followed by cooling down naturally to room temperature. The powders collected were labelled as N-C and were used for the non-contact pyrolysis.

Chemical vapor deposition: 80 mg of anhydrous $FeCl_3$ was placed in a boat in a tube at the upstream of the gas flow. 80 mg of N-C was placed in another boat in the form of a thin layer. There is a 1cm-gap between the two boats with one end cutting off. The furnace was heated up to a variety of temperatures with a ramping rate of 25 °C per minute, and then the temperature was held at a target temperature (T) for three hours, followed by cooling down to room temperature naturally. The furnace was continuously flowed with Ar gas with a flow rate of 0.65 $L \cdot min^{-1}$ during the heating and cooling. The powders were then collected from the N-C boat, and subject to magnetic purification by slowly moving a small magnet ~ 0.5 cm above to remove Fe nanoparticles. The purified powders were labelled FeNC-CVD-T. The powders were stored in a vacuum desiccator before subject to RDE and PEMFC evaluations.

Electrochemical characterization-RDE. The catalyst powders were deposited on a glassy carbon working electrode. Catalyst inks were prepared by dispersing 10 mg of the catalyst powder in a mixture of Millipore water (36.5 μL, 18.2 MΩ cm) and ethanol (300 μL, Sigma-Aldrich, 99.8%), into which 5 wt% Nafion solution (108.5 μL, Sigma-Aldrich) was added as a binder phase. The resulting mixture was sonicated for 60 mins in an ice bath, and then an aliquot of 8.8 μL was drop-cast onto the glassy carbon electrode (0.247 cm^2, Pine instrument), resulting in a loading of 800 $\mu g \cdot cm^{-2}$. The working electrode with the deposited catalyst layer was used in a three-electrode cell set-up connected to a bipotentiostat (Biologic SP 300) and rotator (Pine Instruments). A graphite rod and reversible hydrogen electrode (RHE) were used as counter and reference electrodes, respectively. The ORR performance was evaluated *via* steady-state RDE polarization in O_2-saturated 0.5 M H_2SO_4 using a rotation rate of 900 *rpm*, 20-mV

potential steps from 0.05 to 0.95 V, and a 25-s potential hold time at each step at room temperature. The cyclic voltammetry (*CV*) was carried out between 0.05 to 0.95 V *vs.* RHE with a scan rate of 10 $mV \cdot s^{-1}$ in Ar-saturated 0.5 M H_2SO_4 electrolyte. On the other hand, the ORR performance of Pt/C was evaluated in O_2-saturated 0.1 M $HClO_4$ using a rotation rate of 900 *rpm* and a scan rate of 10 $mV \cdot s^{-1}$ at room temperature. The ORR polarization curve was corrected by the *CV* obtained by scanning the electrode between 0.05 to 0.95 V *vs.* RHE with a scan rate of 10 $mV \cdot s^{-1}$ in Ar-saturated 0.1 M $HClO_4$. The hydrogen underpotential (H_{UPD}) charge was determined by integrating the H_{UPD} peaks in the potential range of 0.05-0.45 V.

Electrochemical characterization-Fuel cell. The FeNC-CVD-750 catalyst was used to prepare the cathode for MEA tests in a PEMFC under H_2-O_2 and H_2-air conditions. The cathode catalyst inks were prepared by dispersing calculated amount of catalyst powder and Nafion D521 dispersion (Ion power) into 50 wt/% 1-propanol aqueous solution for 3 hours under ice bath sonication. The inks were coated layer by layer on SGL 29-BC gas diffusion layer (Sigracet) until 6 $mg \cdot cm^{-2}$ loading was achieved. A commercial Pt gas diffusion electrode (0.3 $mg_{Pt} \cdot cm^{-2}$, fuel cell store) was used as the anode. The anode electrode was first hot pressed onto NR212 membrane (Ion Power) at 130 ^oC for 4 minutes. Before hot pressing the cathode on the opposite side of the membrane, a thin Nafion overspray layer was applied on the cathode catalyst layer to reduce the interfacial resistance. The cathode was then hot pressed on the previously-pressed half MEA at 130 ^oC for 2 minutes. The MEA was then assembled into a single cell with single-serpentine flow channels. The single cell was then evaluated in a fuel cell test station (100 W, Scribner 850e, Scribner Associates). The cells were conditioned under N_2 environment, at

100% relative humidity and 80 °C for at 2 hours. Oxygen flowing at 1000 $ml \cdot min^{-1}$ and H_2 (purity 99.999%) flowing at 200 $ml \cdot min^{-1}$ were used as the cathode and anode reactants, respectively. The back pressures during the fuel cell tests are 1.0 bar reactant gas. The vapor pressure is around 0.5 bar owing to the 100% relative humidity. Thus, the total pressure applied to the MEA is around 1.5 bar (150 KPa). Fuel cell polarization curves were recorded in a voltage control mode.

The H_2-air performance of FeNC-CVD-750 was evaluated in a differential cell owing to its superior mass transport of air. The protocol is otherwise largely the same as that applied for the H_2-O_2 PEMFC evaluation. Few differences include (1) the cathode FeNC-CVD-750 catalyst loading was 4 $mg \cdot cm^{-2}$; (2) the anode loading was 0.2 $mg_{Pt} \cdot cm^{-2}$; and (3) air flowing at 1000 $ml \cdot min^{-1}$ and H_2 (purity 99.999%) flowing at 200 $ml \cdot min^{-1}$ were used as the cathode and anode reactants, respectively.

Physical characterizations.

Inductively coupled plasma optical emission spectrometry (ICP-OES): The ICP-OES tests were conducted at Robertson Microlit Laboratories.

TEM: Transmission electron microscope (TEM) image of the ZIF-8 was conducted on a JEOL 2010 field emission gun (FEG).

STEM: Aberration-corrected scanning transmission electron microscopy (AC-STEM) was conducted using a JEOL NEOARM TEM/STEM operated at 80keV and equipped with a Gatan Quantum electron energy loss spectrometer and dual $100m^2$ silicon drift detectors for energy dispersive X-ray spectroscopy.

SEM: Scanning electron microscopy (SEM) micrographs of N-C were obtained with a Hitachi S-4800 apparatus (Hitachi, Tokyo, Japan).

XRD: X-ray diffraction (XRD) patterns were conducted using a PANanalytical X'Pert Pro powder X-ray diffractometer with Cu K_α radiation.

XPS: X-ray photoelectron spectroscopy (XPS) tests were done with Kratos AXIS Ultra DLD spectrometer with Al Kα (1486.6 eV) X-ray source at UCLA.

N_2 adsorption/desorption analysis*:* N_2 sorption analysis was performed at liquid nitrogen temperature (77 K) with a Micromeritics ASAP 2020 instrument. Prior to the measurements, all samples were degassed at 200 °C for 5 h in flowing nitrogen to remove guest molecules or moisture. The pore size distributions were calculated by fitting the full isotherm with the quench solid density functional theory model with slit pore geometry from NovaWin (Quantachrome Instruments).

Mössbauer spectroscopy*:* ^{57}Fe Mössbauer spectroscopy was used to obtain information on iron speciation. Samples of ~300 mg were mounted in a 2 cm^2 holder. Mössbauer spectra were measured at 5 K in a helium flow cryostat (SHI-850 Series from Janis, USA). The Mössbauer spectrometer (Wissel, Germany) was operated in the transmission mode with a ^{57}Co: Rh source at room temperature. The velocity driver was operated in the constant acceleration mode with a triangular velocity waveform. The velocity scale was calibrated with the magnetically split sextet of a high-purity α-Fe foil at room temperature. The spectra were fitted to appropriate combinations of Lorentzian profiles representing quadrupole doublets and sextets by least-squares methods. Isomer shifts are given relative to α-Fe at room temperature.

XAS measurements**.** The *ex situ* XAS measurements at the Zn K-edge of Zn(II)Pc, ZIF-8, and N-C were performed in transmission mode at beamline 10-ID of the Materials Research Collaborative Access Team (MRCAT) at the Advanced Photon Source, Argonne National Laboratory, Lemont, Illinois, United States. *Ex situ* XAS measurements at the Fe K-edge of Fe-based catalysts were conducted at beamline ISS 6-BM and 8-ID in fluorescence mode in National Synchrotron Light Source II (NSLS-II) (Brookhaven National Laboratory, NY). In addition, *in situ* XAS measurements were conducted on FeNC-CVD-750. The ink for the XAS electrode was composed of 1:3 (wt%) 18.2 MΩ purity deionized water (Millipore) and 2-propanol (HPLC-grade, Aldrich), a 5 wt% Nafion solution (Aldrich), and FeNC-CVD-750 catalyst powder. The inks were directly sprayed onto a Zoltek® carbon cloth on a piece of heated glass. The final Fe loading is ~0.05 $mg_{Fe} \cdot cm^{-2}$ in the electrodes (1×3 cm^2). *Ex situ* XAS data were firstly collected on the dry electrode, which was then conditioned in 0.5 M H_2SO_4 under vacuum for three hours to remove the oxides, impurities, and gases trapped inside the electrode, and to thoroughly wet the electrodes. Afterwards, the electrode was mounted onto a electrochemical half-cell reported previously *(46)* and further conditioned electrochemically for 50 cycles between 0.05 and 0.95 V with a scan rate of 50 mV s^{-1} in N_2-saturated 0.5 M H_2SO_4 electrolyte. Full range Fe K-edge spectra were taken at various static potentials along the anodic sweep of the cyclic voltammetry *(CV)* in O_2-saturated 0.5 M H_2SO_4 electrolyte. Data were collected in fluorescence mode with a Fe reference foil positioned between I2 and I3 as a reference. The voltage cycling limits were 0.50 to 0.95 V vs. RHE. The XAS data were processed and fitted using the Ifeffit−based Athena and Artemis programs *(47)*. Scans were calibrated, aligned, and normalized with

background removed using the IFEFFIT suite *(47)*. The χ(R) were modeled using single scattering paths calculated by FEFF6 *(48)*.

Results and Discussions.

Table S1. Summary of the fitting results of the FT-EXAFS spectra collected at the Zn K-edge of the in-house ZIF-8, commercial Zn(II)Pc, and the Zn in the ZIF-8-derived N-C.

Zn-N bond	R (Å)	N	$\sigma^2 \times 10^{-3}$ (Å^2)	E_0 (eV)
ZIF-8	1.99(1)	4.1(5)	6(2)	4(1)
Zn(II)Pc	1.98(1)	3.8(8)	4(2)	5(2)
N-C	2.00(1)	4.8(5)	12(2)	3(1)

*Fits were done at the Zn K-edge in *R*-space, $k^{1,2,3}$ weighting. $1.0 < R < 2.0$ Å and Δk = 2.275 – 10.61 Å^{-1}. S_0^2 was fixed at 0.95 obtained by fitting the reference Zn foil. The number given in the parentheses represents the uncertainty of the last digit of the fitting result.

Table S2. Element contents in the N-C and FeNC-CVD-T determined by ICP-OES.

wt%	Fe	Zn	N	C
N-C	-	2.16	4.23	84.00
FeNC-CVD-650	2.25	1.05	3.97	85.42
FeNC-CVD-750	2.00	0.12	4.24	85.48
FeNC-CVD-900	3.76	0.23	3.32	85.42
FeNC-CVD-1000	2.72	0.03	2.36	84.20

Table S3. Parameters obtained from fitting the Mössbauer spectrum of FeNC-CVD-750 acquired at 5 K (**Figure 2D**): relative area (RA, %), isomer shift (IS, mm s^{-1}), quadrupole splitting (QS, mm s^{-1}), and line width (LW, mm s^{-1}) of each component.

Comp.	RA %	IS mm s^{-1}	QS mm s^{-1}	LW mm s^{-1}	Assignment
Doublet 1	89	0.50	1.02	1.25	O_2-Fe(III)-N_4
Doublet 3	11	0.97	3.56	0.92	$FeCl_2$

Table S4. Summary of the fitting results of the FT-EXAFS spectra collected at the K-edge of the FeNC-CVD-750 *ex situ* exposed to air or at 0.9 V in O_2-saturated 0.5 M H_2SO_4*

	R (Å)	N	$\sigma^2 \times 10^{-3}$ (Å^2)	E_0 (eV)
Ex situ	2.02(1)	5.9(9)	6(2)	0.7(1.0)

0.9 V	2.00(2)	6(1)	6(4)	-1(1)

*Fits were done at the Fe K-edge in *R*-space, $k^{1,2,3}$ weighting. 1.0 < *R* < 2.1 Å and Δk = 2.3 – 11.0 $Å^{-1}$ were used for fitting. S_0^2 was fixed at 0.81 obtained by fitting the reference foil. The number given in the parentheses represents the uncertainty of the last digit of the fitting result.

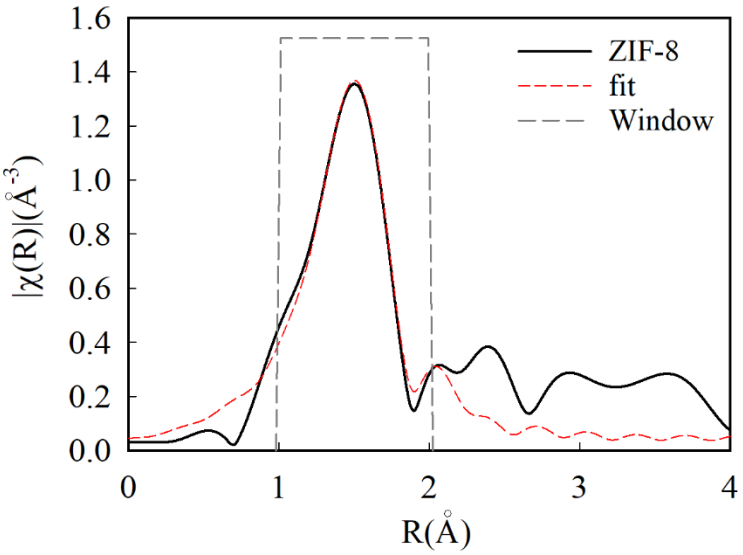

Figure S1. FT-EXAFS spectra of the synthesized ZIF-8 at the Zn K-edge with the corresponding fit. The fitting results are listed in Table S1.

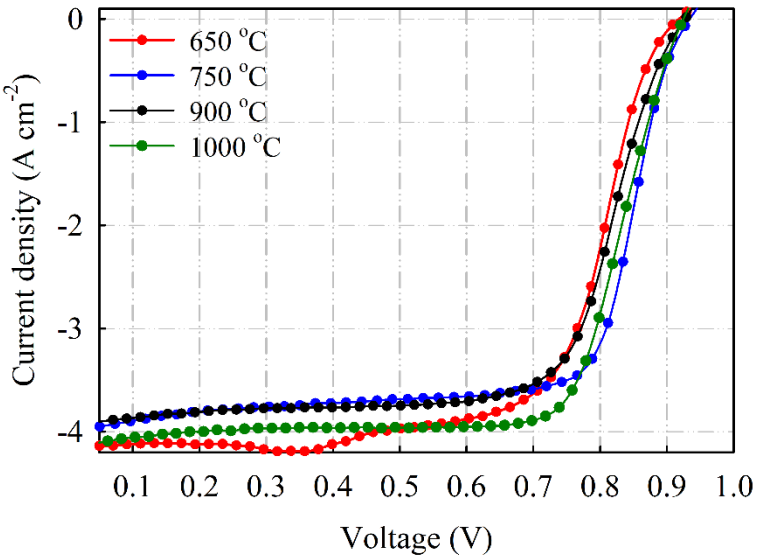

Figure S2. Steady-state RDE polarization in O_2-saturated 0.5 M H_2SO_4 at room temperature using a rotation rate of 900 *rpm*, 20 mV potential steps from 0.05 to 0.95 V, and a 25 s potential hold time at each step.

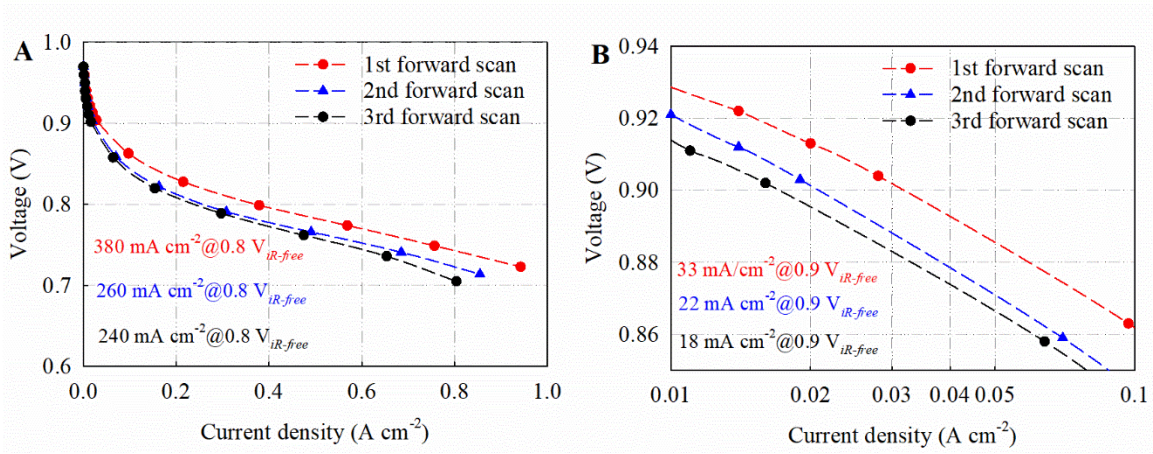

Figure S3. The first three forward scans of the H_2-O_2 PEMFC polarization with *i*R-correction. Cathode: ~6.0 mg·cm^{-2} of the FeNC-CVD-750 catalyst; Anode: 0.3 mg$_{Pt}$·cm^{-2} Pt/C; Membrane: Nafion 212; 200·mL/min^{-1} gas fed at both anode (H_2) and cathode (O_2) with 100% RH, and 1.0 bar partial pressure each side; cell 80°C; electrode area 5 cm^2.

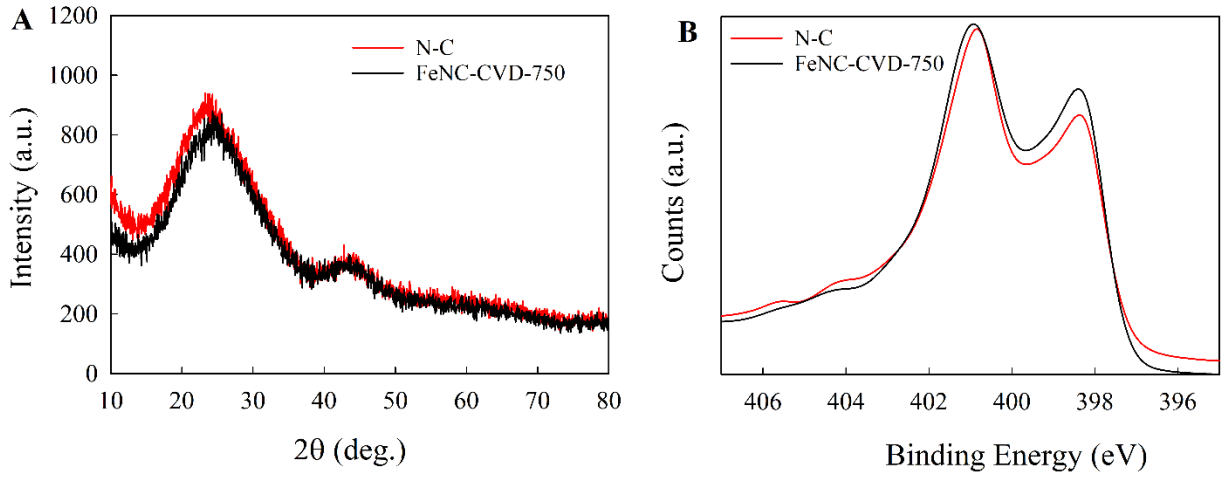

Figure S4. **(A)** XRD spectra of N-C and FeNC-CVD-750. **(B)** XPS N1s spectra of N-C and FeNC-CVD-750.

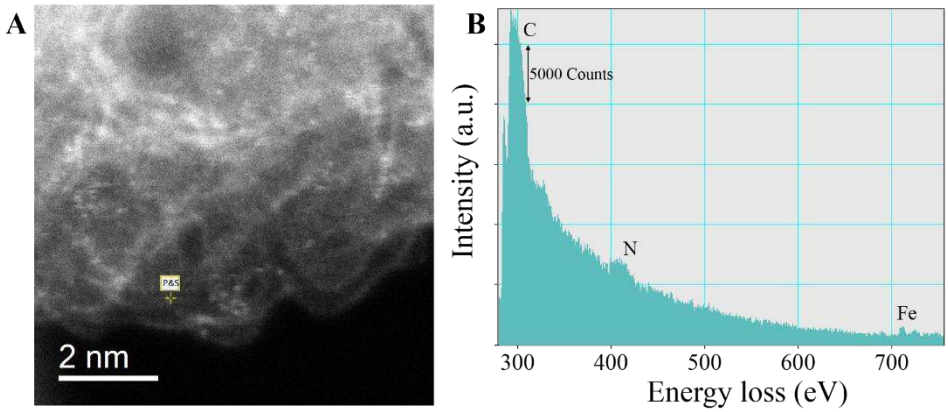

Figure S5. (**A**) High resolution ADF-STEM image of FeNC-CVD-750. (**B**) EEL spectrum of the N k-edge and Fe L-edge acquired from single atoms highlighted in (A).

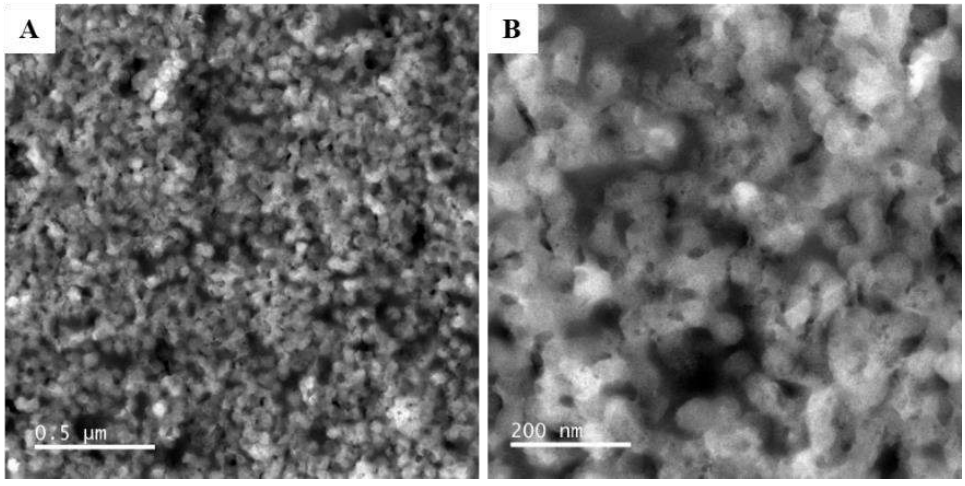

Figure S6. ADF-STEM images of the cathode of the MEA.

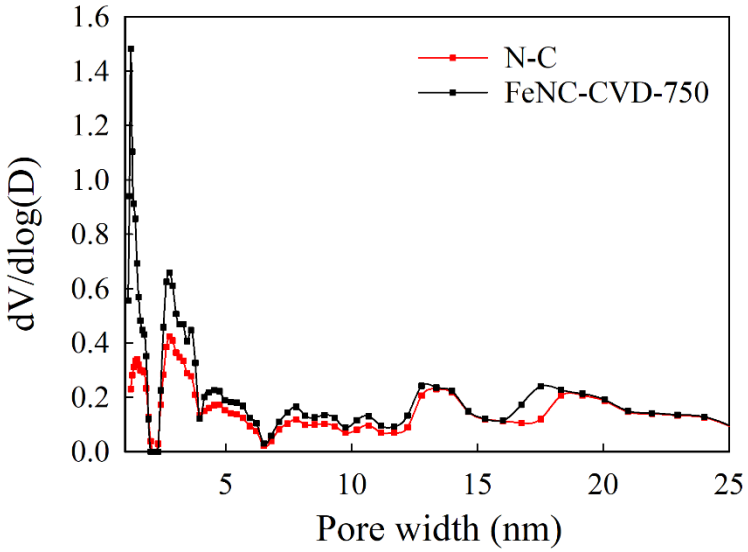

Figure S7. Micropore and mesopore size distributions. dV/dlog (D) is the differential pore volume distribution, where V is pore volume and D is pore diameter.

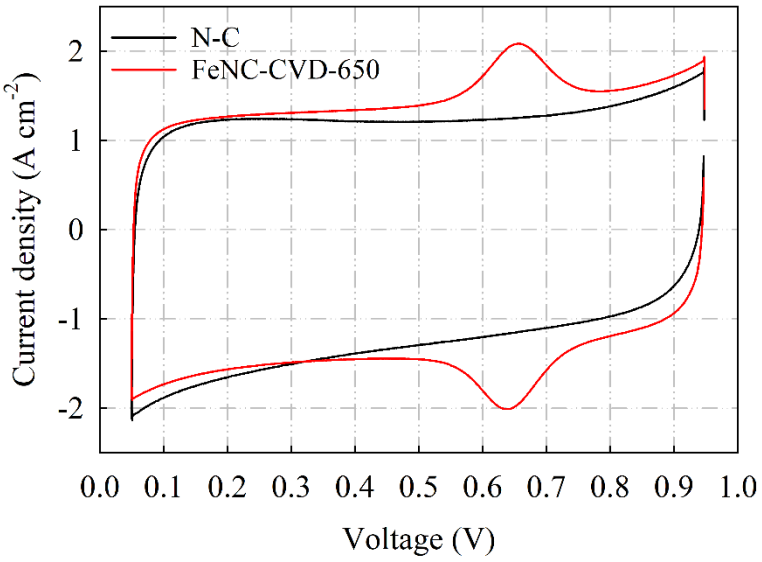

Figure S8. Cyclic voltammograms (*CVs*) of the FeNC-CVD-750 and N-C collected in an Ar-saturated 0.5 M H_2SO_4 electrolyte at room temperature with a scan rate of 10 $mV \cdot s^{-1}$.

Calculations of the SD_{mass} and TOFs of FeNC-CVD-750.

The electrochemically active Fe-N_4 site density (*S.D.*) on the RDE electrode of FeNC-CVD-750 is calculated from the electric charge derived from the area of the FeII/FeIII redox peak (A_{redox} = 2.55×10^{-4} A·V·cm^{-2}) in the *CV* present in Figure 4A by the following equation:

$$S.D. = \frac{A_{redox}[A \cdot V \cdot cm^{-2}] \times N_A[atom \cdot mol^{-1}]}{W[V \cdot s^{-1}] \times F[s \cdot A \cdot mol^{-1}]} = 1.6 \times 10^{17}(sites \cdot cm^{-2})$$

(S1)

assuming one active Fe-N_4 site transfer one electron during the Fe(II)/Fe(III) redox transition. N_A is Avogadro's constant; F is Faraday constant; and W is the scan rate of the *CV* (Figure 3D) (0.01 V·s^{-1}).

The SD_{mass} of FeNC-CVD-750 is determined by dividing the *S.D.* by the mass of the FeNC-CVD-750 catalyst on the RDE electrode per electrode area (L = 800 μg·cm^{-2} or 8×10^{-4} g·cm^{-2}):

$$SD_{mass} = \frac{S.D[sites \cdot cm^{-2}]}{L\ [g \cdot cm^{-2}]} = 2 \times 10^{20}(sites \cdot g^{-1})$$

(S2)

The Fe utilization (U_{Fe}) is in turn derived from the *S.D.* and the Fe loading on the RDE electrode with the following equation:

$$U_{Fe} = \frac{S.D[sites \cdot cm^{-2}] \times M_{Fe}[g \cdot mol^{-1}]}{L\ [g \cdot cm^{-2}] \times Fe\ wt\% \times N_A[atom \cdot mol^{-1}]} = 92\%$$

(S3)

Wherein M_{Fe} is the molar mass of iron; and the Fe wt% is 2 wt_{Fe}%.

The TOF ($e^{-}\cdot site^{-1}\cdot s^{-1}$, at 0.8 V) is calculated from the i_k (25 $A\cdot g^{-1}$) at 0.8 V and SD_{mass} based on the following equation:

$$TOF = \frac{i_k@0.8\,V\ [A\cdot g^{-1}]\times N_A[site\cdot mol^{-1}]}{SD_{mass}[sites\cdot g^{-1}]\times F[s\cdot A\cdot mol^{-1}]} = 0.78\ (e^{-}\cdot site^{-1}\cdot s^{-1}) \quad \text{(S4)}$$

References

45. Q. Jia, W. Liang, M. K. Bates, P. Mani, W. Lee, S. Mukerjee, Activity descriptor identification for oxygen reduction on platinum-based bimetallic nanoparticles: in situ observation of the linear composition–strain–activity relationship. *ACS Nano* **9**, 387-400 (2015).

46. M. Newville, IFEFFIT : interactive XAFS analysis and FEFF fitting. *J. Synchrotron Radiat.* **8**, 322-324 (2001).

47. A. L. Ankudinov, B. Ravel, J. J. Rehr, S. D. Conradson, Real-space multiple-scattering calculation and interpretation of x-ray-absorption near-edge structure. *Phys. Rev. B* **58**, 7565-7576 (1998).